Spectroscopic Definition of the Copper Active Sites in Mordenite: Selective Methane Oxidation

9 AUTHORS, INCLUDING:

Pieter Vanelderen
University of Leuven
12 PUBLICATIONS **301** CITATIONS

SEE PROFILE

Ryan G Hadt
Argonne National Laboratory
33 PUBLICATIONS **949** CITATIONS

SEE PROFILE

Robert A Schoonheydt
University of Leuven
307 PUBLICATIONS **9,153** CITATIONS

SEE PROFILE

Bert F Sels
University of Leuven
187 PUBLICATIONS **5,570** CITATIONS

SEE PROFILE

Spectroscopic Definition of the Copper Active Sites in Mordenite: Selective Methane Oxidation

Pieter Vanelderen,[†,‡,∥] Benjamin E. R. Snyder,[†,∥] Ming-Li Tsai,[†] Ryan G. Hadt,[†] Julie Vancauwenbergh,[‡] Olivier Coussens,[‡] Robert A. Schoonheydt,*[,‡] Bert F. Sels,*[,‡] and Edward I. Solomon*[,†]

[†]Department of Chemistry, Stanford University, Stanford, California 94305, United States
[‡]Center for Surface Chemistry and Catalysis, KU Leuven, Kasteelpark Arenberg 23, 3000 Leuven, Belgium

Ⓢ Supporting Information

ABSTRACT: Two distinct $[Cu-O-Cu]^{2+}$ sites with methane monooxygenase activity are identified in the zeolite Cu-MOR, emphasizing that this Cu-O-Cu active site geometry, having a ∠Cu-O-Cu ~140°, is particularly formed and stabilized in zeolite topologies. Whereas in ZSM-5 a similar $[Cu-O-Cu]^{2+}$ active site is located in the intersection of the two 10 membered rings, Cu-MOR provides two distinct local structures, situated in the 8 membered ring windows of the side pockets. Despite their structural similarity, as ascertained by electronic absorption and resonance Raman spectroscopy, the two Cu-O-Cu active sites in Cu-MOR clearly show different kinetic behaviors in selective methane oxidation. This difference in reactivity is too large to be ascribed to subtle differences in the ground states of the Cu-O-Cu sites, indicating the zeolite lattice tunes their reactivity through second-sphere effects. The MOR lattice is therefore functionally analogous to the active site pocket of a metalloenzyme, demonstrating that both the active site and its framework environment contribute to and direct reactivity in transition metal ion-zeolites.
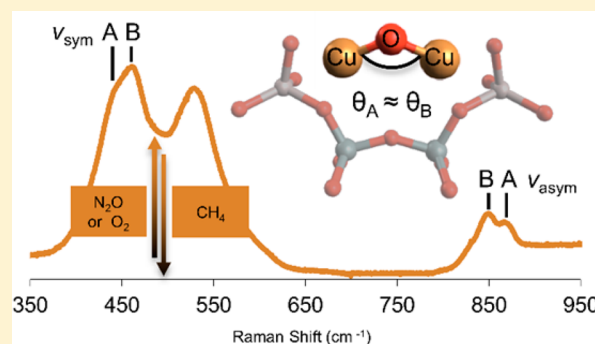
1. INTRODUCTION

The selective oxidation of hydrocarbons to oxygenated products is an extremely challenging, yet economically important reaction. It requires very selective catalysts with high activity at sufficiently low temperatures to avoid excessive formation of CO and CO_2. Methane is a particularly challenging substrate due to its high C-H bond strength (104 kcal/mol), and only a limited number of natural and synthetic systems are capable of catalyzing this reaction.[1−5] Soluble methane monooxygenase and particulate methane monooxygenase (pMMO) are, respectively, Fe- and Cu-containing enzymes that selectively convert methane to methanol at room temperature, thus fulfilling the conditions of high activity and excellent selectivity at low temperature.[6,7] To date, the reactive intermediate of the copper-containing pMMO has not been identified, as its reactive state is difficult to generate and trap in solution.[7−11] Zeolites, on the other hand, are microporous materials that can stabilize exceptionally reactive, well-defined Fe/O and Cu/O sites.[12,13]

Zeolite-bound Fe/O and Cu/O sites that selectively oxidize methane to methanol have been identified.[14−18] Cu-ZSM-5 is one such system.[19−21] Cu-ZSM-5 can oxidize methane to methanol at low temperature (<200 °C) using O_2 from the atmosphere. The methanol produced remains chemisorbed (presumably as methoxide[22]), and can be removed with an appropriate solvent or by steam treatment.

Woertink et al.[20] determined that the active Cu site in Cu-ZSM-5 was a new species in Cu/O chemistry using resonance Raman (rR) spectroscopy, a site-selective method that enabled the distinction of the 5 mol % active site from 95 mol % spectator Cu. The reactive copper site is characterized by an absorption band at 22 700 cm^{-1}. Tuning a laser into this absorption feature resonantly enhances vibrations associated with the active site. rR vibrations at 237 cm^{-1}, 456 and 870 cm^{-1} were assigned as the Cu-O-Cu bending mode, the symmetric Cu-oxo stretch (ν_s) and antisymmetric Cu-oxo stretch (ν_{as}), respectively, of a bent mono(μ-oxo)dicopper site (140° ∠CuOCu). Essential for this assignment was a feature at 1725 cm^{-1}, which is the second quantum of the antisymmetric stretch. It is more intense than the fundamental because it is symmetric, and therefore rR allowed. In analogy to previously characterized Fe-O-Fe sites,[23] the manifestation of strong symmetric and weak antisymmetric stretches led to the assignment of a bent Cu-O-Cu core in Cu-ZSM-5.

The capacity of the ZSM-5 lattice to host a $[Cu_2O]^{2+}$ core was evaluated with density functional theory (DFT) calculations. The best description is a $[Cu_2O]^{2+}$ core bound to the Al T-sites of an Al-$(SiO)_2$-Al sequence within the 10 membered ring (MR) of ZSM-5, with each Cu coordinated in a bidentate fashion to the zeolite lattice. The calculated E_a for the reaction

of this copper core toward methane is 18.5 kcal/mol, which is in reasonable agreement with the experimental value of 15.7 kcal/mol. Moreover, the DFT study showed that the reactivity has its origin in the strength of the O−H bond produced, which provides a strong driving force, and the polarization of a frontier MO toward a Cu^I-oxyl radical at the transition state.[20]

To date, the $[Cu_2O]^{2+}$ core of Cu-ZSM-5 is one of only two characterized intermediates in the methane to methanol reaction.[20,24] Its discovery has had a broad impact on the fields of heterogeneous catalysis and bioinorganic chemistry.[25−28] The specific ZSM-5 structure is expected to be a critical factor in the stabilization of the active $[Cu_2O]^{2+}$ site, but aspects of the ZSM-5 topology that stabilize Cu$_2$O cores are not fully understood. Studying other zeolite topologies should enable identification of structures that stabilize and activate Cu-oxo species. This would provide insight into the influence of the zeolite lattice on active site geometry and reactivity.

Recently, there is increased interest in Cu-MOR, which is also capable of selectively oxidizing methane to methanol.[19,29−32] Literature suggests a high density of active sites for Cu-MOR,[29,31] and the larger pores of the MOR framework are favorable for product desorption and transportation. Analogous to Cu-ZSM-5, O$_2$-activated Cu-MOR has an absorption feature in the 22000 cm^{-1} region.[16] A similar active copper site is expected, but not yet evidenced.[29] In a recent study, we examined the copper distribution in relation to the redox chemistry and spectroscopic features of Cu-MOR.[29] It was found that 60% of all coppers, including the 22 200 cm^{-1} related species, undergo autoreduction, in good agreement with the amount of copper that changes structure during methane reaction obtained from in situ XAS experiments by van Bokhoven et al.[31] The same group also showed that the active species can be generated and consumed in a batch-wise operation mode, with product release by steam treatment.[32]

Here, we provide definitive evidence of the formation of $[Cu_2O]^{2+}$ cores in Cu-MOR. Experimental insight is obtained from in situ diffuse reflectance UV−vis and rR data, which are presented in combination with a CH$_4$ reactivity study. These data are then compared to previous studies on Cu-ZSM-5. While the geometric and electronic structures of the $[Cu_2O]^{2+}$ cores in the two zeolites are highly similar, their reactivity differs, indicating the participation of the zeolite lattice in the reaction coordinate. This combined catalytic and spectroscopic study represents an important step forward in understanding general principles governing the geometric and electronic structure and reactivity of zeolite-bound $[Cu_2O]^{2+}$ sites.

2. MATERIALS AND METHODS

2.1. Sample Preparation. The parent sodium mordenite (Südchemie; Si/Al = 5) was subjected to an extra ion exchange in a sodium nitrate (NaNO$_3$) solution to ensure the mordenite was completely in its sodium form prior to copper cation exchange. This ensures a maximized copper exchange and prevents side reactions with Brönsted acid sites or lewis acid extra-framework aluminum sites[33] created by dehydration of Brönsted acid sites during high temperature treatments. Ion-exchange was performed with an aqueous solution of Cu(II)-acetate, (Cu(CH$_3$CO$_2$)$_2$·H$_2$O), at ambient temperature for 24 h. The Cu^{2+} exchange was repeated three times, with a washing step in between. After the third exchange, the samples were washed and dried at 80 °C. The Cu and Al contents were determined by an ICP analysis. The Cu content was 0.71 mmol/g and the Cu/Al ratio was 0.43. The samples were pelletized to obtain grain sizes between 0.25 and 0.50 mm diameter.

2.2. Sample Activation. The standard pretreatment consists of a calcination in O$_2$ at 450 °C for 2 h (1 °C/min), followed by He treatment at 500 °C overnight. The standard pretreatment is either followed by a pure O$_2$ treatment at 250 °C overnight or by dosing N$_2$O (5% in Helium) at 250 °C for 5 min.

^{18}O labeled active copper sites were achieved by five cycles of autoreduction in He at 500 °C and ^{18}O$_2$ activation at 250 °C. This method was applied to saturate the zeolite lattice with ^{18}O atoms, since ^{18}O isotope exchange of TMI oxygen sites with the lattice ^{16}O atoms has been observed for TMI zeolites.[34,35]

2.3. UV−Vis-NIR and rRaman Spectroscopy. All treatments prior to in situ UV−vis-NIR rR spectroscopic measurements were performed in a quartz U-tube/flow cell. The latter was equipped with a window for in situ UV−vis-NIR diffuse reflectance spectroscopy (DRS) and a side arm for in situ rRaman measurements. After UV−vis measurement, the catalyst pellets were mounted in the quartz side arm of the U-tube, ensuring that the conditions for UV−vis-NIR and resonance Raman measurements were identical. It should be emphasized that all successive steps were done in situ and that samples never came in contact with air.

DRS spectra were recorded on a Varian Cary 5000 UV−VIS−NIR spectrophotometer at room temperature against a halon white reflectance standard in the range 4000−50000 cm^{-1}. Resonance Raman (rR) spectra were recorded using a Spex 1877 CP triple monochromator with 1200, 1800, and 2400 grooves/mm holographic spectrograph gratings and an Andor Newton CCD cooled to −80 °C. Excitation was provided by either a Coherent I90C−K Kr$^+$ ion laser (λ_{ex} = 407 nm, 488 nm, 588 nm) or an Innova Sabre 25/7 Ar$^+$ CW ion laser (λ_{ex} = 351 nm, 457.9 nm). The spectral resolution was ∼2 cm^{-1}. Spectra were recorded at room temperature. Baseline spectra were collected from a sample of Cu-MOR containing no CH$_4$-reactive sites.

2.4. Operando UV−Vis Study. Kinetic studies were conducted by means of a set up that allowed spectral changes to be monitored during the reaction. The reactions were carried out in a fixed bed reactor. The setup consists of a plug flow reactor (id = 8 mm) fitted inside a furnace, a UV−Vis light source (Top Sensor Systems DH-2000 deuterium halogen light source) and a photodiode array detector (Ocean Optics SD 2000) connected to the catalyst bed via optical fiber technology (Top Sensor Systems FCB-UV400 ME cable and FCB-UV400G-0.1-XHT high temperature probe). Each spectrum is the result of the superposition of 300 scans in the 38000−12000 cm^{-1} region, each 50 ms in duration.

A total amount of 0.3 g of Cu−MOR catalyst (with an average crystal size of 1 μm) was pelletized to obtain grain sizes between 0.25 and 0.50 mm diameter and loaded in a quartz reactor (with a reactor volume, 1 cm^3). The catalyst was then exposed to a flow of pure oxygen (2 h at 450 °C), followed by a He treatment overnight at 500 °C. The reactor was cooled to 250 °C and contacted with a flow of N$_2$O in He (50 cm^3/min; 5 vol %). Subsequently, the reactor was cooled to the reaction temperature, ranging from 50 to 200 °C, and contacted with a flow of CH$_4$ in He (50 cm^3/min; 10 vol %).

2.5. Temperature-Programmed Desorption. A 0.2 g amount of Cu−MOR catalyst (with an average crystal size of 1 μm) was pelletized to obtain grain sizes between 0.25 and 0.50 mm diameter and loaded in a quartz reactor (with a reactor volume, 1 cm^3). Cu-MOR was activated with O$_2$ at 250 °C (vide supra). Subsequently, the activated Cu-MOR is heated (5 °C/min) in a He flow (20 mL/min). The gas flow at the reactor outlet is analyzed with a quadrupole mass spectrometer. Mass 32 was monitored to measure the O$_2$ release from the Cu-MOR surface as a function of the temperature.

3. RESULTS AND ANALYSIS

3.1. In Situ Diffuse Reflectance UV−Vis Study.
3.1.1. Catalyst Activation. Cu-MOR (Si/Al = 5) with an atomic Cu/Al ratio of 0.43 was prepared according to the procedure described in the Materials and Methods section. After synthesis, the sample was calcined in O$_2$ at 450 °C for 2h, followed by a He treatment at 500 °C overnight. The sample was then oxidized by either O$_2$ or N$_2$O at 250 °C, and

subsequently reacted with methane at 150 °C. Figure 1 shows the UV−vis absorption spectra after O_2 treatment and
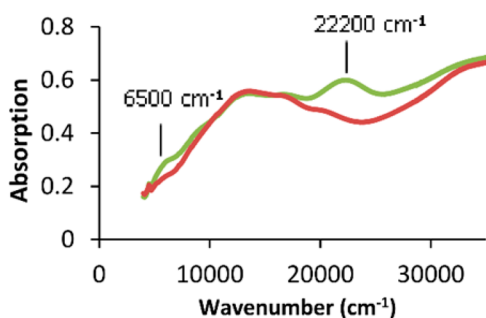

Figure 1. Cu-MOR sample after O_2 activation at 250 °C (green) and after subsequent methane reaction at 150 °C (red).

subsequent methane reaction. O_2 treatment at 250 °C results in a maximized intensity of the 22 200 cm^{-1} absorption (Abs) band. This band is related to the methane oxidizing copper site as it disappears during the methane reaction at 150 °C. It is also notable that a small absorption feature around 6500 cm^{-1} disappears together with the 22200 cm^{-1} band. Similar spectral changes have been reported for Cu-ZSM-5. The same spectrum was obtained for the N_2O treatment, see Supporting Information Figure S1.

3.1.2. Stability in Oxidizing Atmosphere. The stability of sites contributing to the 22 200 cm^{-1} absorption feature was assessed by monitoring the Abs feature while heating (5 °C/min) a sample in an O_2 flow to 450 °C after O_2 activation at 250 °C. Figure 2A shows the behavior of the 22200 cm^{-1} band between 300 and 450 °C, the interval between the spectra is 30 °C. A strong decrease of the absorption band was observed above 330 °C, until it stabilized around 420 °C. The difference between the spectra at 300 and 450 °C has a maximum intensity at 21 900 cm^{-1} (Figure 2B, red). After 10 h at 450 °C, the O_2 flow was switched to helium, resulting in the complete disappearance of the remaining component of the Abs feature. The difference between the spectra before and after helium is shown in Figure 2B in black and has its maximum at 23 100 cm^{-1}. These observations suggest that different sites contribute to the 22 200 cm^{-1} feature. One component has an absorption maximum at 21 900 cm^{-1} and appears to be unstable above 330 °C in an O_2 atmosphere, in contrast to a second component that persists in O_2 above 330 °C and has an absorption maximum at 23 100 cm^{-1}.

Interestingly, attempts to restore the 21 900 cm^{-1} absorption band by cooling the sample, containing the 23 100 cm^{-1} species, in O_2 from 450 to 250 °C were unsuccessful. The autoreduction step in helium at 450 °C is necessary to return the catalyst to its initial state, enabling formation of the full absorption band with O_2 at 250 °C. This indicates that the sites contributing to the 21 900 cm^{-1} band are inactivated and not merely desorbed in the higher temperature oxidizing conditions.

3.1.3. Stability in Inert Atmosphere. The thermal stability of the two species in an inert atmosphere was studied by O_2 temperature-programmed desorption (TPD) after O_2 activation at 250 °C. UV−vis absorption spectra were measured at different temperatures. The TPD profile, shown in Figure 3A, revealed two broad partially overlapping O_2 desorption peaks with maxima at 355 and 385 °C. The difference between the absorption spectra obtained after desorption at 310 and 350
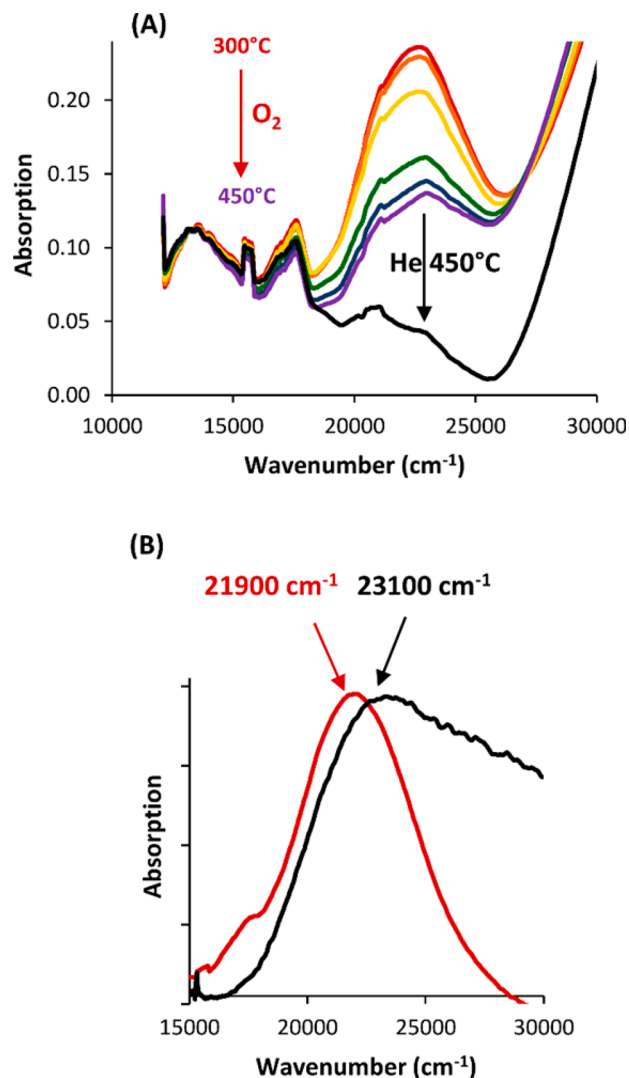

Figure 2. (A) Intensity decrease upon heating a Cu-MOR sample in O_2 flow to 450 °C after O_2 activation at 250 °C; the spectra are measured at, respectively, 300 °C (red), 330 °C (orange), 360 °C (yellow), 390 °C (green), 420 °C (blue), and 450 °C (purple). The spectrum after complete autoreduction in helium flow at 450 °C is shown in black. (B) Difference of two consecutive spectra during heating in O_2 to 450 °C (red) and the difference between the spectrum measured in O_2 at 450 °C and He at 450 °C (black).

°C; and at 350 and 390 °C are shown in Figure 3B,C. The 22 200 cm^{-1} Abs feature is resolved into two bands with maxima at 21 900 and 23 100 cm^{-1}. The intensity decrease of the UV−vis band in the low temperature part of the first desorption peak is largely due to loss of the 23100 cm^{-1} component, as can be seen from the difference spectrum of the UV−vis spectra at 310 and 350 °C (Figure 3B yellow). The 21 900 cm^{-1} band more significantly contributes to the intensity decrease associated with the higher temperature desorption peak (Figure 3C red). Thus, O_2-TPD confirmed the presence of two absorption bands, one at 23 100 cm^{-1} and one at 21 900 cm^{-1}, derived from distinct active sites with slightly different stabilities toward O_2 desorption.

Note that the species stable at high temperature in O_2, i.e., the 23 100 cm^{-1} related site, desorbs at low temperature during TPD. The relative stability of the active sites in an inert atmosphere thus differs from that under oxidizing conditions.
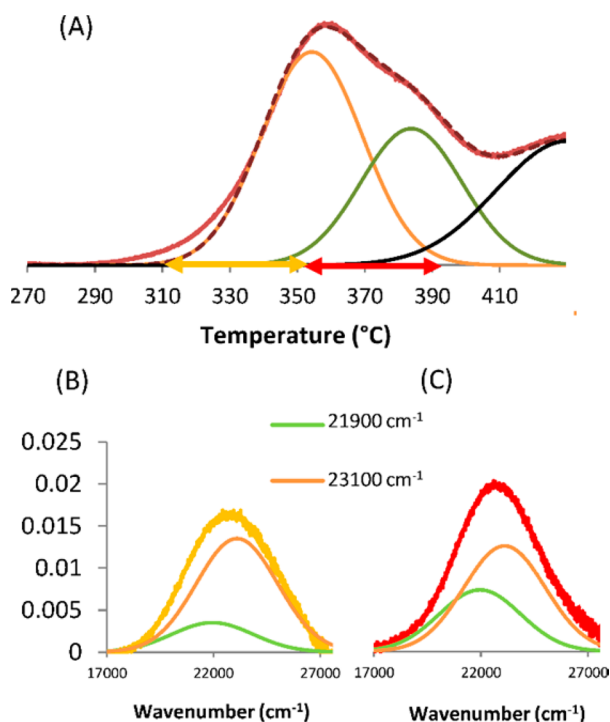
Figure 3. (A) MS signal of O_2 during TPD of an activated Cu-MOR (red) and its fitted peaks (dashed line is the sum). (B) Difference spectrum between absorption spectra at 310 °C and 350° and (C) difference spectrum between absorption spectra at 350 and 390 °C, deconvoluted with absorption maxima at 21 900 and 23 100 cm^{-1}.

Figure 4. Eyring kinetics of CH_4 reaction with activated Cu-MOR. Eyring plots derived from the decay of Cu-MOR's deconvolution bands at 23 100 cm^{-1} (blue) and 21900 cm^{-1} (red) during reaction with CH_4. Error bars indicate the 95% confident interval of the linear regression.

This is explained by the observation that the disappearance of the 21900 cm^{-1} band in O_2 is not a desorption process, but reflects an irreversible conversion of one copper site (vide supra) and thus is not related to the TPD experiment.

3.1.4. Kinetics of CH_4 Reaction. Differences in the geometric and electronic structure of the two active sites of Cu-MOR may lead to differences in reactivity toward CH_4. To assess this possibility, differences in reactivity were quantified by monitoring the disappearance of the 22 200 cm^{-1} absorption envelope during CH_4 reaction at different temperatures ranging from 90 to 200 °C. Loss of individual components of the Abs feature (at 21 900 and 23 100 cm^{-1}) was monitored by a Gaussian deconvolution of the 22 200 cm^{-1} band envelope. The decay of the absorption bands as a function of time was evaluated with the first-order rate equation:

$$\ln(\mathrm{Abs}_0 - \mathrm{Abs}_f)/\mathrm{Abs}_t - \mathrm{Abs}_f) = kt$$

Abs_0, Abs_f, and Abs_t are the intensities of the absorption bands at the start, finish and time t of the reaction, respectively. The plot of $\ln(\mathrm{Abs}_0 - \mathrm{Abs}_f)/\mathrm{Abs}_t - \mathrm{Abs}_f)$ as a function of time is a straight line for which the slope is the rate constant (k) at that particular temperature (Supporting Information Figure S3). The change of $\ln(k/T)$ as a function of $1000/T$ was used to construct Eyring plots for both copper oxygen sites, shown in Figure 4. From these Eyring plots the following activation enthalpy $\Delta H^{\ddagger}$ and activation entropy $\Delta S^{\ddagger}$ were obtained:

- 21 900 cm^{-1} absorption related copper site: $\Delta H^{\ddagger}$ = 14.7 $\pm$ 0.5 kcal mol^{-1} and $\Delta S^{\ddagger}$ = −36 $\pm$ 1.5 cal mol^{-1} K^{-1}
- 23 100 cm^{-1} absorption related copper site: $\Delta H^{\ddagger}$ = 11.1 $\pm$ 0.5 kcal mol^{-1} and $\Delta S^{\ddagger}$ = −44 $\pm$ 1.5 cal mol^{-1} K^{-1}

On the basis of the slopes of the Eyring plots, it is clear that the two sites have different activation enthalpies for methane
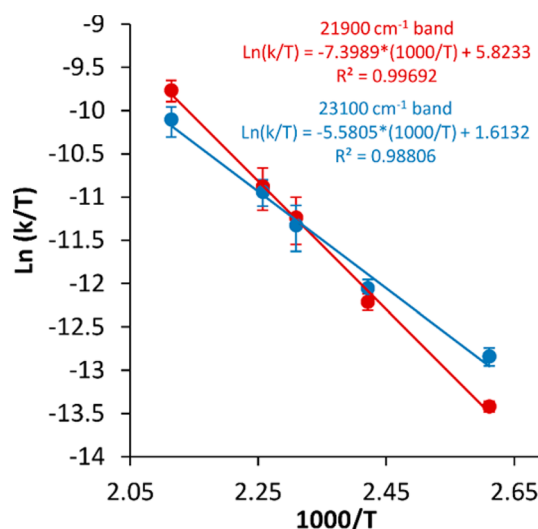
oxidation. It is noteworthy that the Eyring plots obtained for Cu-MOR have a common intersection point, with an isokinetic temperature at 160 °C. An isokinetic temperature in an Eyring plot is often explained in the literature by a compensation effect, whereby different enthalpies of activation are compensated by differences in the entropies of activation. However, a number of other factors may lead to isokinetic points, so this observation should be interpreted cautiously.

3.2. Resonance Raman. The 22000 cm^{-1} absorption feature of activated Cu-MOR is uniquely identified with the CH_4 reactive sites. Tuning a laser into the 22000 cm^{-1} absorption feature resonantly enhances a number of vibrations (Figure 5) that are not present before activation, disappear upon reaction with CH_4, and are demonstrated to profile the 22000 cm^{-1} Abs feature (Figure 6). These features are therefore correlated with the sites that contribute to the 22000 cm^{-1} Abs feature. O_2- and N_2O-activated samples yield the same resonance Raman (rR) features, demonstrating the same active sites are formed upon activation with either O_2 or N_2O (Supporting Information Figure S5).

The rR spectrum of activated Cu-MOR strongly resembles that of activated Cu-ZSM-5 (Figure 5). As with Cu-ZSM-5, isotope sensitive features are seen at 455 ($\Delta^{16}O/^{18}O$ = 5−8) cm^{-1}, ∼850 ($\Delta^{16}O/^{18}O$ = 40) cm^{-1}, 1700 ($\Delta^{16}O/^{18}O$ = 70−80) cm^{-1}, and 1850 ($\Delta^{16}O/^{18}O$ = 30) cm^{-1} (Figure 7). While similar frequencies and isotope shifts are observed for Cu-ZSM-5, the MOR features are broad and asymmetric, suggesting more than one species is present. This limits the quantitative analysis of isotope shifts for Cu-MOR.

The rR profile spectra of the 22 000 cm^{-1} Abs feature of activated Cu-MOR confirm the presence of multiple active sites. The 22 000 cm^{-1} Abs feature contains two components at 21 900 and 23 100 cm^{-1} (vide supra). Tuning a laser into the high-energy shoulder of the Abs feature is therefore expected to more strongly enhance vibrations associated with the 23 100 cm^{-1} component. Conversely, tuning a laser into the low energy shoulder is expected to more strongly enhance vibrations associated with the 21 900 cm^{-1} component. This behavior is observed experimentally: the shape of each rR
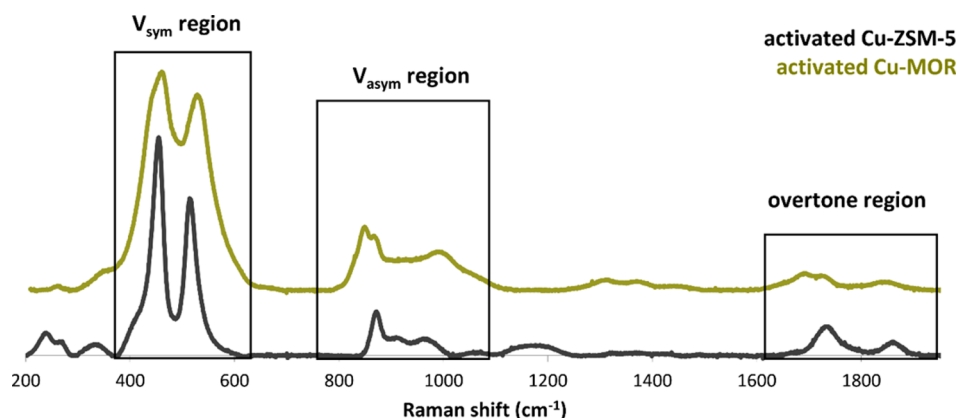
Figure 5. Comparison of the resonance Raman spectra (λ_{ex} = 458 nm) of O_2 activated Cu-MOR and Cu-ZSM-5.
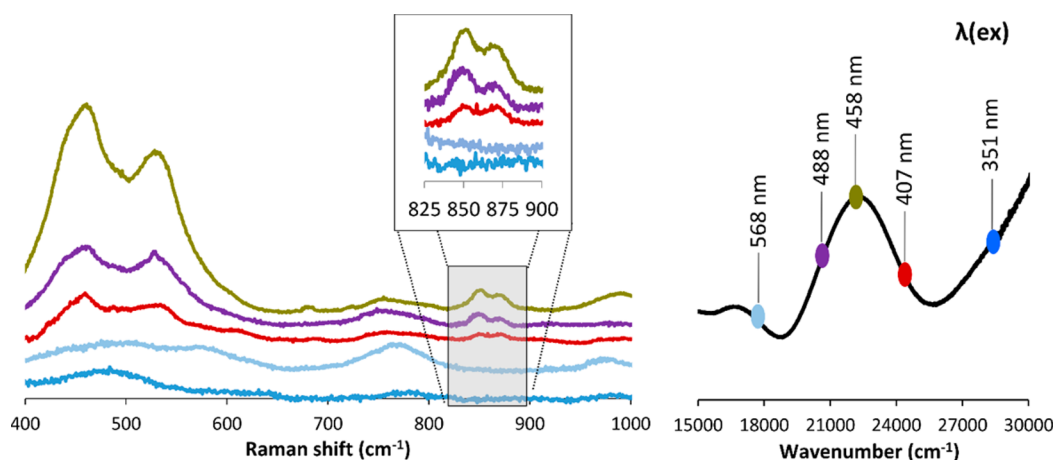

Figure 6. Resonance Raman spectra of N_2O-activated Cu-MOR collected at various excitation energies (left). Note the shift in relative intensity of the features between 825 and 900 cm^{-1} (left). The different laser excitation lines (in nm) are indicated on the absorption spectrum of an O_2 activated MOR (right).
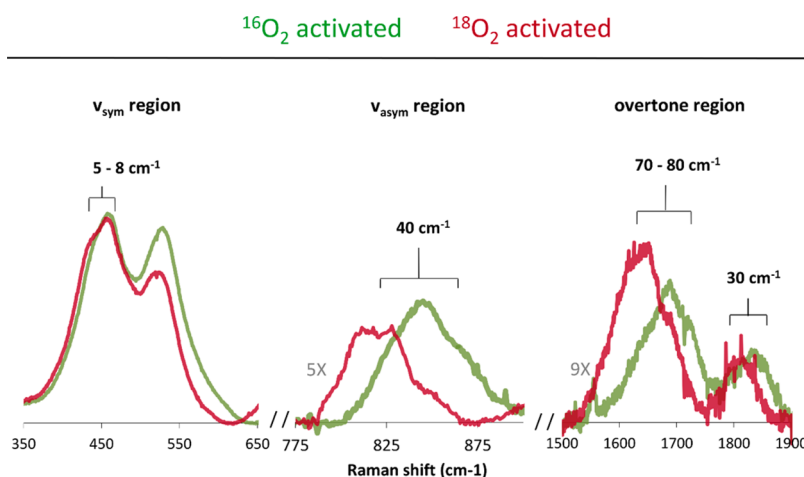

Figure 7. Resonance Raman spectra (λ_{ex} = 458 nm) of Cu-MOR activated with $^{18}O_2$ (red) and subsequent $^{16}O_2$ activation (green).

feature identified above is sensitive to excitation energy. Consider the feature at ~850 cm^{-1} (Figure 6, inset). At low excitation energies, the lower frequency component is most prominent. The relative intensity of this component decreases with increasing excitation energy, however. Similar behavior is observed for the prominent asymmetric features at 460 cm^{-1} and 530 cm^{-1}, indicating each of these features is a also a composite.

The profiling behavior and asymmetry of the rR features of activated Cu-MOR indicate two Cu/O active sites are formed in Cu-MOR. Each rR feature is therefore a composite of vibrations from separate sites. Features of the individual sites could not be accurately distinguished based on the differential enhancement observed during profiling studies. Alternatively, they could be distinguished by differential reactivity of the sites with CH_4. Kinetics data (Figure 4) indicate the site associated
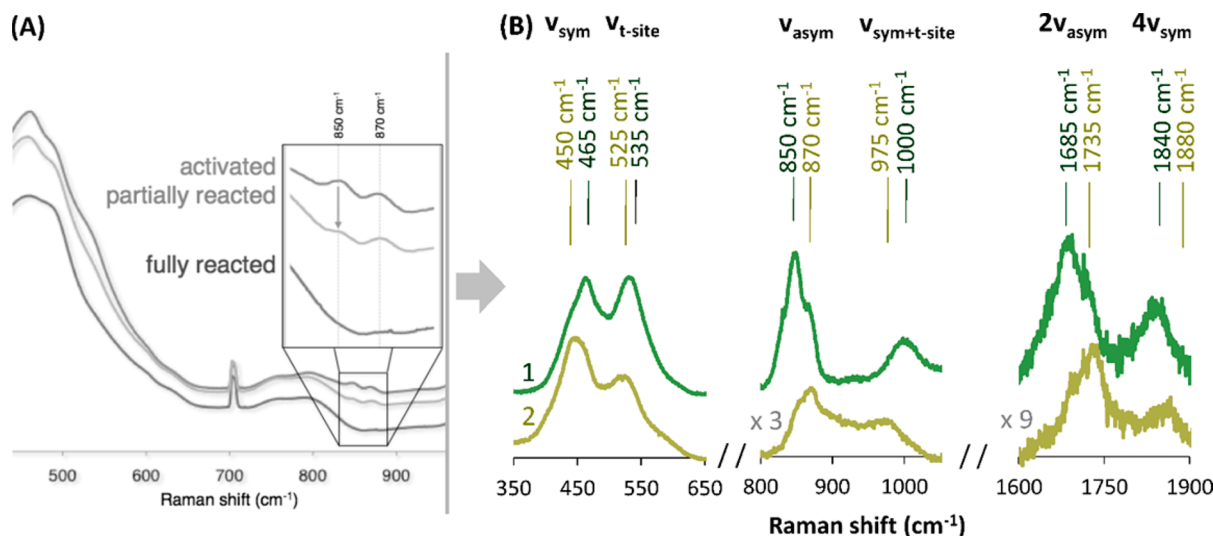
Figure 8. (A) Resonance Raman spectra (λ_{ex} = 458 nm) of activated Cu-MOR during reaction with CH_4 at 200 °C. Note the relative decrease of the 850 cm^{-1} vibration after partial reaction. (B) rR spectra of individual MOR sites 1 (green) and 2 (yellow) generated by subtraction of spectra from activated and partially reacted samples (λ_{ex} = 458 nm).

with the 21900 cm^{-1} absorption feature reacts ∼60% more rapidly with CH_4 at 200 °C than the site associated with the 23 100 cm^{-1} absorption feature. A sample of activated Cu-MOR was therefore exposed to a pulse of CH_4 (contact time: 20 s) at 200 °C, and rR data collected before and after partial CH_4 reaction were compared (Figure 8). After baseline correcting these spectra against a fully CH_4-reacted sample, the rR features of the individual MOR sites were distinguished through spectral subtraction. A constant multiple of the partially reacted spectrum was subtracted from the unreacted spectrum. The constant was increased systematically until only one set of features dominated. A small contribution of the subtracted species was kept to prevent oversubtraction. The process of spectral subtraction is expected to introduce uncertainties on the order of ±5 cm^{-1} to the frequencies reported in the difference spectra shown in Figure 8. The difference spectra enable distinction of rR features of the individual $[Cu_2O]^{2+}$ sites in MOR. The prominent symmetric stretch at 465 cm^{-1} is correlated to the antisymmetric stretch at 850 cm^{-1} (related to the 21 900 cm^{-1} absorption band) and the symmetric stretch at 450 cm^{-1} to the antisymmetric stretch at 870 cm^{-1} (related to the 23 100 cm^{-1} absorption band).

The CH_4 reactivity and characteristic spectroscopic features of the individual Cu-MOR sites have thus been identified, demonstrating that activated Cu-MOR contains two distinct mono-oxo-bridged Cu dimers. The 21900 and 23100 cm^{-1} components of the Abs feature of Cu-MOR are therefore assigned as oxo → Cu(II) ligand-to-metal charge transfers (LMCTs), and the rR vibrations of the individual MOR sites are assigned in analogy to our past study of Cu-ZSM-5.[20] The frequencies and isotope sensitivities of ν_{sym} and ν_{asym} were related to the bridge angle and Cu–O$_{oxo}$ bond strengths of each $[Cu_2O]^{2+}$ core (Table 1) using a normal coordinate analysis (NCA) as given by the equations of Wing and Callahan for a triatomic M–O–M unit with C_{2v} symmetry.[36] The NCA indicates that the $[Cu_2O]^{2+}$ cores of Cu-MOR and Cu-ZSM-5 are comparable, yielding highly similar estimates of Cu–O bond strengths and bridge angles for the three sites. The subtle differences in ν_{sym}/ν_{as} for MOR 1 versus MOR 2 reflect limited differences in ∠CuOCu and Cu–O force constant. This

Table 1. Summary of rR Features and NCA of ZSM-5 and MOR Sites

	ZSM-5	MOR 1	MOR 2
ν_{sym} (cm^{-1})	456	465	450
ν_{asym} (cm^{-1})	870	850	870
∠CuOCu (deg)	140	137	141
Cu–O$_{oxo}$ FC (mdyn/Å)	3.8	3.7	3.8
Cu–O$_{oxo}$/ Cu–O$_{oxo}$ interaction FC: k_{MOM} (mdyn/Å)	0.25	0.25	0.25

analysis is robust. While spectral subtraction introduces uncertainties of up to ±5 cm^{-1} for ν_{sym} and ν_{asym}, this has a minimal impact on the structural parameters estimated by this NCA (e.g., ±1 deg for <CuOCu and ±0.1 mdyne/Å for the Cu–O force constant (FC)).

4. DISCUSSION

Previous studies of activated Cu-ZSM-5 identified characteristic spectral features of a bent $[Cu_2O]^{2+}$ site that exhibits selective, low temperature H atom abstraction (HAA) reactivity with CH_4. The mono(μ-oxo) dicopper site in ZSM-5 was, until now, the only characterized Cu/O site capable of selective methane oxidation.[20,25] It has now been demonstrated that $[Cu_2O]^{2+}$ cores are also responsible for the low-temperature, selective CH_4 reactivity of activated Cu-MOR. Unlike ZSM-5, however, the MOR topology stabilizes two distinct $[Cu_2O]^{2+}$ sites. These sites exhibit characteristic spectral features and reactivities similar to ZSM-5. The intense absorption feature of activated Cu-MOR (around 22000 cm^{-1}) is assigned as a composite of two oxo → Cu(II) LMCTs, each associated with a specific site. Tuning a laser into this absorption feature resonantly enhances vibrations characteristic of bent $[Cu_2O]^{2+}$ sites: an intense symmetric stretching mode of the bridging oxo ligand at 440–470 (^{16}O/^{18}O = 5–10) cm^{-1}, and the corresponding weak antisymmetric stretch between 850 and 870 (^{16}O/^{18}O = 40) cm^{-1}. NCA of the frequencies of these modes indicate the bond strengths and Cu–O–Cu bridge angles for the MOR and ZSM-5 sites are similar. Similarities between the spectral features and reactivity of the MOR- and ZSM-5-bound

$[Cu_2O]^{2+}$ sites indicate that they have comparable geometric and electronic structures. These are summarized in Table 2.

Table 2. Summary of Spectroscopic Features and CH$_4$ Reactivities of ZSM-5 and MOR-Bound $[Cu_2O]^{2+}$ Sites

	ZSM-5	MOR 1	MOR 2
O$_2$ TPD peak	390 °C	385 °C	355 °C
Stability in O$_2$ at 450 °C	stable	unstable	stable
Absorption feature (cm^{-1})	22700	21900	23100
CH$_4$ $\Delta H^{\ddagger}$ (kcal/mol)	15.7	14.7	11.1
CH$_4$ $\Delta S^{\ddagger}$ (cal/(mol K))	−35	−36	−44
CH$_4$ $\Delta G^{\ddagger}$ @ 200 °C	32.0	31.6	31.9
ν_{sym} (cm^{-1})	456	465	450
ν_{asym} (cm^{-1})	870	850	870
<CuOCu (deg)	140	137	141
Cu−O force constant (mdyne/Å)	3.8	3.7	3.8

That these Cu$_2$O cores have very similar geometric and electronic structures is interesting given the different topologies of the MOR and ZSM-5 lattices. Though a larger Cu−O−Cu angle might be expected from the larger diameter of the 12 MR in MOR compared to the 10 MR in ZSM-5, the apparent tendency to solely form the observed geometry implies that a particular structural entity, present in both zeolites, uniquely stabilizes $[Cu_2O]^{2+}$ cores. This is consistent with our recent DFT study on Cu-ZSM-5,[37] where it was found that, from all the possible 2Cu^I precursor sites in the 10 MR, there is one that is particularly stable. Moreover, the Cu−O−Cu site derived from this 2Cu^I had the best fit with the experimental spectral features. The 2Cu^I precursor site is shown in Figure 9. In the
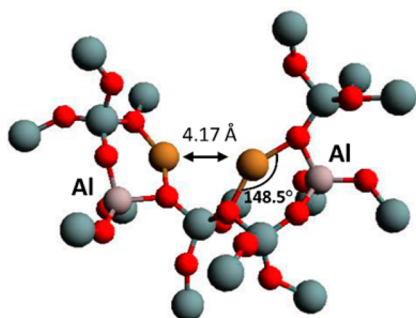

Figure 9. Structural model for the binuclear Cu^I precursor (in yellow) of the Cu−O−Cu site in ZSM-5.[37] Si atoms are in gray and oxygen atoms in red.

same study the Cu−O−Cu site formation from the 2Cu^I precursor with N$_2$O was evaluated. N$_2$O, instead of O$_2$, was used since the generation of the Cu−O−Cu core then involves only one O atom and only two electrons. Only a sufficiently short Cu−Cu distance (<4.2 Å) will allow N$_2$O bridging, enabling 2 electron activation to form the Cu$_2$O core with a low barrier (2 kcal/mol). The Cu^I centers prefer bidentate coordination with a close to linear O$_{lat}$−Cu−O$_{lat}$ bite angle. The two coordinate Cu^I geometry with 150° bite angles is provided by the ZSM-5 lattice by binding a Cu^I ion to a lattice oxygen ligand from an Al T site and the other from a Si T site. These lattice oxygens therefore are separated by the appropriate distance by the curvature of the 10MR.

A comparison of the crystal structures of MOR and the MFI topology of ZSM-5 reveals key similarities between local structures where the 2Cu^I precursor site can be formed. The mordenite structure is built from the same 5−1 secondary building unit[38] as ZSM-5; both framework structures are shown in Figure 10. The MOR structure contains straight 12 MR channels (7 × 6.5 Å), with parallel compressed 8 MR channels (5.7 × 2.6 Å). The 12 MR and 8 MR channels are connected by another 8MR channel, creating the so-called side pockets with 8 MR windows (3.4 × 4.8 Å). Two neighboring 12 MR channels do not have a direct connection and the side pockets are staggered at the intersection with the 8 MR channels. As a result of this structural organization, diffusion of molecules only takes place in one dimension, i.e., along the 12MR channel. MOR is therefore considered as a 1D zeolite. The mordenite unit cell has four distinct tetrahedral sites: T1 in the 12 membered ring (MR) channel, T2 and T4 at the intersection of the 12MR channel with the side- pocket and T3 at the intersection of the 8MR channel with the side pocket.[38] ZSM-5 has a 3D pore system that consists of straight 10 MR channels (5.1 × 5.5 Å), connected by sinusoidal 10 MR channels (5.3 × 5.6 Å). Calcined ZSM-5 has 24 distinct tetrahedral sites in its asymmetric unit.[38]

There are two positions in the 12MR mordenite channel with a conformation of lattice O atoms similar to the local environment of the Cu^I ions in ZSM-5 shown in Figure 9. This is illustrated in Supporting Information Figure S6 by placing Cu^I ions (in yellow) with bite angles of 150° at these two positions. Lattice O atoms from other nearest neighbor T-sites are about 0.3 Å too far from each other to achieve similar bite angles. One Cu^I position is at a T4 site (indicated in green) and, as illustrated in Figure 11, placing a second symmetrically equivalent Cu^I ion opposite to it in the side pocket results in a Cu^I pair coordinated to two T4 sites (indicated in green) separated by two T2 sites. These two T4 atoms are separated by 7.54 A, which is equivalent to the local structure around the
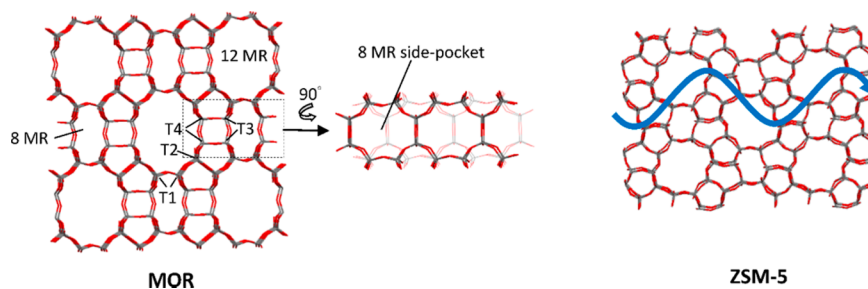

Figure 10. Framework structures of mordenite (left) and ZSM-5 (right). Si atoms are in gray and O atoms are in red. The four nonequivalent tetrahedral sites of mordenite are indicated on the structure. The blue arrow indicates the sinusoidal 10 MR channel in ZSM-5.
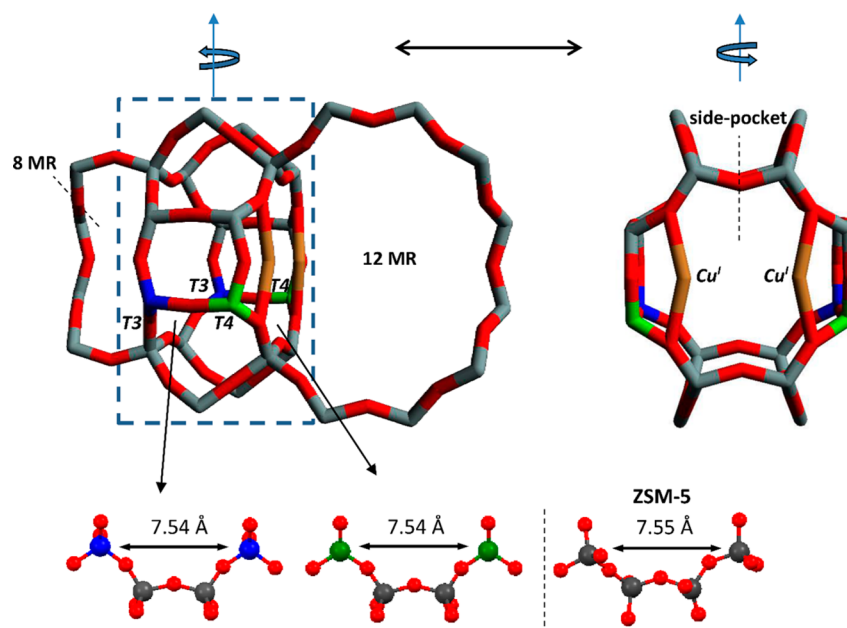
Figure 11. (Top) Local structures of the MOR lattice at the intersection of the side-pocket with the 12 MR and 8 MR channels. T4 and T3 atoms of a possible Al−Si−Si−Al configurations for Cu−O−Cu coordination are indicated respectively in green and blue. A pair of Cu^I atoms (yellow) with bite angles of 150° is placed at two T4 sites. Oxygen atoms at the outside of the 8MR and 12MR are omitted for clarity. (Bottom) Comparison the local structure stabilizing the Cu−O−Cu site in ZSM-5 with the T4-T2-T2-T4 and T3-T2-T2-T3 sequences in MOR. The distance between two T atoms with hypothetical Al substitution is indicated.

active site in activated Cu-ZSM-5 (7.55 A), as shown in Figure 11 (bottom right). The striking resemblance with ZSM-5 makes the side pocket at the intersection with the 12MR a promising candidate to host one Cu−O−Cu site. Note that a highly similar configuration of T sites is found at the intersection of the side pocket with the 8MR, viz. two T3 sites (Figure 11 in blue) separated by two T1 sites. Several binding modes of Cu^I in the confined space of the compressed 8 MR channel can be envisioned. One possibility, analogous to that presented in Figure 11, is shown in Supporting Information Figure S7.

There is consensus that Al is substituted preferentially at the T3 and T4 sites (ca. 30−45% occupancy by Al for Si/Al = 5), while the percent occupation of Al at T1 and T2 is relatively low (ca. 5−10%).[39−43] The combination of Al-pairs and the proper local structure seems the ideal recipe for the formation and stabilization of the active Cu−O−Cu moieties in zeolites. It appears that this configuration in the zeolite lattice provides the appropriate positioning of Cu^I pairs required to form the Cu−O−Cu site, and in addition provides a structure that stabilizes the Cu−O−Cu site once it is formed. Thus, Al$_{T3}$−O−Si$_{T1}$−O−Si$_{T1}$−O−Al$_{T3}$ and Al$_{T4}$−O−Si$_{T2}$−O−Si$_{T2}$−O−Al$_{T2}$ sequences are particularly attractive candidates to stabilize Cu−O−Cu cores. On the basis of the higher Al occupancy of T3 relative to T4, it is likely that MOR 2 (the major species by O$_2$ TPD) is stabilized by a pair of T3 Al sites, and is thus buried deep within the side pocket. The minor species, MOR 1, is likely stabilized by a pair of T4 Al sites, and is therefore exposed directly to the 12MR channel. Reactivity studies that will test this model and experimentally define the locations of MOR 1 and MOR 2 are now in progress.

The substantial similarities between the ZSM-5 and MOR-bound [Cu$_2$O]$^{2+}$ sites defined experimentally suggest ZSM-5 and MOR-bound [Cu$_2$O]$^{2+}$ sites exhibit exceptional reactivity toward CH$_4$ for similar reasons. Previous DFT studies of Cu-

ZSM-5 defined two key contributions to the low barrier for HAA from CH$_4$ by a [Cu$_2$O]$^{2+}$ core.[20] First, the approaching substrate polarizes the reactive LUMOs of the core toward the bridging oxo ligand, generating a Cu(I)-oxyl-like electronic structure. This enhances the electrophilicity of the bridging oxo, activating it toward HAA. The second contribution to the low barrier comes from the high strength of the O−H bond in the resulting [Cu$_2$OH]$^{2+}$ first product.

Although [Cu$_2$O]$^{2+}$ sites bound to ZSM-5 and MOR are likely reactive with CH$_4$ for the same reasons, one of these sites (MOR 2) exhibits a 3.6−4.6 kcal/mol lower $\Delta H^{\ddagger}$ for the CH$_4$ oxidation. This difference in reactivity is too large to be explained by the subtle differences in the MOR-bound [Cu$_2$O]$^{2+}$ cores defined experimentally. However, the [Cu$_2$O]$^{2+}$ site with the lower $\Delta H^{\ddagger}$ (MOR 2 in Table 2) has a significantly higher $\Delta S^{\ddagger}$, consistent with a more confined reaction environment, again suggesting MOR 2 is located deep inside the side pocket coordinated to a pair of Al T3 sites (see Figure 11 in blue). The lower $\Delta H^{\ddagger}$ may therefore be related to the influence of the zeolite lattice on the HAA reaction coordinate. If an active site is located in a constricted space (e.g., in the side pockets or 8MR of MOR), the lattice may influence the trajectory of CH$_4$ approach. In this case, substrate confinement may influence $\Delta H^{\ddagger}$. For a confined core, second sphere lattice O atoms could stabilize/destabilize the HAA transition state and/or the [Cu$_2$OH]$^{2+}$ first product; or even enable a more activated [Cu$_2$O]$^{2+}$ geometry to form along the CH$_4$ reaction coordinate.

On the basis of the above considerations, the zeolite lattice appears functionally analogous to the active-site pocket of a metalloenzyme. For example: tyrosinase, catechol oxidase, and hemocyanin all contain planar μ−η^2:η^2 peroxo-bridged dicopper cores with very similar spectral features, yet each enzyme exhibits substantially different reactivity.[44] This differ-ence in reactivity is attributed to the influence of the active site

pocket (e.g., second sphere residues) on substrate approach and interaction with the $[Cu_2(O_2)]^{2+}$ core. The MOR lattice likely exerts an analogous influence on the CH_4 HAA reaction for at least one of the MOR-bound $[Cu_2O]^{2+}$ sites. Computational studies will enable assignment of these sites to specific 8MR windows and define the origin of their differential reactivity with CH_4.

5. CONCLUSION

For the first time, the active species in Cu-MOR have been unambiguously identified. It was found that there are in fact two $[Cu_2O]^{2+}$ sites present. These two sites are highly similar to each other and to the active $[Cu_2O]^{2+}$ site in ZSM-5. This observation suggests a conserved structural motif is present in both the ZSM-5 and MOR topologies that stabilizes the $[Cu_2O]^{2+}$ geometries defined experimentally. The two windows of the 8MR side pocket in MOR are appealing candidates given their resemblance to the local structure around the Cu−O−Cu site in ZSM-5. Testing a range of zeolites might further demonstrate that only zeolites with a similar local structure stabilize $[Cu_2O]^{2+}$ sites capable of the CH_4 to CH_3OH reaction.

It is unlikely that the difference in reactivity between the two $[Cu_2O]^{2+}$ sites in mordenite is due to small differences in their ground states defined experimentally. Instead, it appears that the zeolite lattice contributes to the reactivity of one of these sites (MOR 2), e.g., by directing the approach of methane to the active sites, or by influencing the stability of the products and/or HAA transition state. The zeolite lattice may therefore be functionally analogous to the active site pocket of a metalloenzyme. A detailed computational analysis of the MOR active sites will elaborate this analogy, further developing the correspondence between biological and heterogeneous Cu/O sites that exhibit selective, low-temperature reactivity with methane.

ASSOCIATED CONTENT

Ⓢ Supporting Information

UV−vis−NIR and resonance Raman spectra of Cu-MOR after N_2O activation, kinetics of the 22000 cm^{-1} absorption band during reaction met methane and additional Cu-MOR structures are available. The Supporting Information is available free of charge on the ACS Publications website at DOI: 10.1021/jacs.5b02817.

AUTHOR INFORMATION

Corresponding Authors
*edward.solomon@stanford.edu
*robert.schoonheydt@biw.kuleuven.be
*bert.sels@biw.kuleuven.be

Author Contributions
‖These authors contributed equally.

Notes
The authors declare no competing financial interest.

ACKNOWLEDGMENTS

REFERENCES

(1) Hermans, I.; Spier, E. S.; Neuenschwander, U.; Turrà, N.; Baiker, A. *Top. Catal.* **2009**, *52*, 1162.
(2) Hammond, C.; Conrad, S.; Hermans, I. *ChemSusChem* **2012**, *5*, 1668.
(3) Sun, M.; Zhang, J.; Putaj, P.; Caps, V.; Lefebvre, F.; Pelletier, J.; Basset, J.-M. *Chem. Rev.* **2014**, *114*, 981.
(4) Shilov, A. E.; Shteinman, A. A. *Russ. Chem. Rev.* **2012**, *81*, 291.
(5) Schwarz, H. *Angew. Chem., Int. Ed.* **2011**, *50*, 10096.
(6) Shu, L.; Nesheim, J. C.; Kauffmann, K.; Münck, E.; Lipscomb, J. D.; Que, L. *Science* **1997**, *275*, 515.
(7) Lieberman, R. L.; Rosenzweig, A. C. *Nature* **2005**, *434*, 177.
(8) Balasubramanian, R.; Smith, S. M.; Rawat, S.; Yatsunyk, L. A.; Stemmler, T. L.; Rosenzweig, A. C. *Nature* **2010**, *465*, 115.
(9) Balasubramanian, R.; Rosenzweig, A. C. *Acc. Chem. Res.* **2007**, *40*, 573.
(10) Himes, R. A.; Barnese, K.; Karlin, K. D. *Angew. Chem., Int. Ed.* **2010**, *49*, 6714.
(11) Himes, R. A.; Karlin, K. D. *Curr. Opin. Chem. Biol.* **2009**, *13*, 119.
(12) Vanelderen, P.; Vancauwenbergh, J.; Sels, B. F.; Schoonheydt, R. A. *Coord. Chem. Rev.* **2013**, *257*, 483.
(13) Smeets, P. J.; Woertink, J. S.; Sels, B. F.; Solomon, E. I.; Schoonheydt, R. A. *Inorg. Chem.* **2010**, *49*, 3573.
(14) Sobolev, V. I.; Dubkov, K. A.; Panna, O. V.; Panov, G. I. *Catal. Today* **1995**, *24*, 251.
(15) Starokon, E. V.; Parfenov, M. V.; Pirutko, L. V.; Abornev, S. I.; Panov, G. I. *J. Phys. Chem. C* **2011**, *115*, 2155.
(16) Smeets, P. J.; Groothaert, M. H.; Schoonheydt, R. A. *Catal. Today* **2005**, *110*, 303.
(17) Wulfers, M. J.; Teketel, S.; Ipek, B.; Lobo, R. F. *Chem. Commun.* **2015**, *51*, 4447.
(18) Beznis, N. V.; Weckhuysen, B. M.; Bitter, J. H. *Catal. Lett.* **2010**, *138*, 14.
(19) Groothaert, M. H.; Smeets, P. J.; Sels, B. F.; Jacobs, P. a; Schoonheydt, R. A. *J. Am. Chem. Soc.* **2005**, *127*, 1394.
(20) Woertink, J. S.; Smeets, P. J.; Groothaert, M. H.; Vance, M. A.; Sels, B. F.; Schoonheydt, R. A.; Solomon, E. I. *Proc. Natl. Acad. Sci. U.S.A.* **2009**, *106*, 18908.
(21) Vanelderen, P.; Hadt, R. G.; Smeets, P. J.; Solomon, E. I.; Schoonheydt, R. A.; Sels, B. F. *J. Catal.* **2011**, *284*, 157.
(22) Narsimhan, K.; Michaelis, V. K.; Mathies, G.; Gunther, W. R.; Griffin, R. G.; Roman-Leshkov, Y. *J. Am. Chem. Soc.* **2015**, *137*, 1825.
(23) Czernuszewicz, R. S.; Sheats, J. E.; Spiro, T. G.; Spire, T. G. *Inorg. Chem.* **1987**, *26*, 2063.
(24) Banerjee, R.; Proshlyakov, Y.; Lipscomb, J. D.; Proshlyakov, D. a. *Nature* **2015**, *518*, 431.
(25) Himes, R. A.; Karlin, K. D. *Proc. Natl. Acad. Sci. U.S.A.* **2009**, *106*, 18877.
(26) Haack, P.; Limberg, C.; Ray, K.; Braun, B.; Kuhlmann, U.; Hildebrandt, P.; Herwig, C. *Inorg. Chem.* **2011**, *50*, 2133.
(27) Haack, P.; Kaergel, A.; Greco, C.; Dokic, J.; Braun, B.; Pfaff, F. F.; Mebs, S.; Ray, K.; Limberg, C. *J. Am. Chem. Soc.* **2013**, *135*, 16148.
(28) Haack, P.; Limberg, C. *Angew. Chem., Int. Ed.* **2014**, *53*, 4282.
(29) Vanelderen, P.; Vancauwenbergh, J.; Tsai, M.-L.; Hadt, R. G.; Solomon, E. I.; Schoonheydt, R. a; Sels, B. F. *ChemPhysChem* **2014**, *15*, 91.
(30) Alayon, E. M. C.; Nachtegaal, M.; Bodi, A.; van Bokhoven, J. A. *ACS Catal.* **2014**, *4*, 16.

(31) Alayon, E. M. C.; Nachtegaal, M.; Kleymenov, E.; van Bokhoven, J. A. *Microporous Mesoporous Mater.* **2013**, *166*, 131.

(32) Alayon, E. M.; Nachtegaal, M.; Ranocchiari, M.; van Bokhoven, J. A. *Chem. Commun.* **2012**, *48*, 404.

(33) Copéret, C. *Chem. Rev.* **2010**, *110*, 656.

(34) Valyon, J.; Hall, K. W. *J. Catal.* **1993**, *142*, 520.

(35) Pirngruber, G. D.; Roy, P. K. *Catal. Lett.* **2004**, *93*, 75.

(36) Wing, R. M.; Callahan, K. P. *Inorg. Chem.* **1969**, *8*, 871.

(37) Tsai, M.-L.; Hadt, R. G.; Vanelderen, P.; Sels, B. F.; Schoonheydt, R. a; Solomon, E. I. *J. Am. Chem. Soc.* **2014**, *136*, 3522.

(38) Baerlocher, C.; McCusker, L. B.; Olson, D. H. *Atlas of Zeolite Framework Types*; Elsevier: Amsterdam, The Netherlands, 2007.

(39) Bodart, P.; Nagy, J. B.; Derouane, E. G.; Gabelica, Z. In *Structure and Reactivity of Modified Zeolites*; Jacobs, P. A., Ed.; Elsevier: Amsterdam, 1984; Vol. *18*, pp 125−132.

(40) Bodart, P.; Nagy, J. B.; Debras, G.; Cabelica, Z.; Jacobs, P. A. *J. Phys. Chem.* **1986**, *90*, 5183.

(41) Debras, G.; Nagy, J. B.; Gabelica, Z.; Bodart, P.; Jacobs, P. A. *Chem. Lett.* **1983**, *12*, 199.

(42) Alberti, A. *Zeolites* **1997**, *19*, 411.

(43) Dedecek, J.; Sobalik, Z.; Wichterlova, B.; Děděček, J.; Sobalík, Z.; Wichterlová, B. *Catal. Rev. Sci. Eng.* **2012**, *54*, 135.

(44) Solomon, E. I.; Heppner, D. E.; Johnston, E. M.; Ginsbach, J. W.; Cirera, J.; Qayyum, M.; Kieber-Emmons, M. T.; Kjaergaard, C. H.; Hadt, R. G.; Tian, L. *Chem. Rev.* **2014**, *114*, 3659.